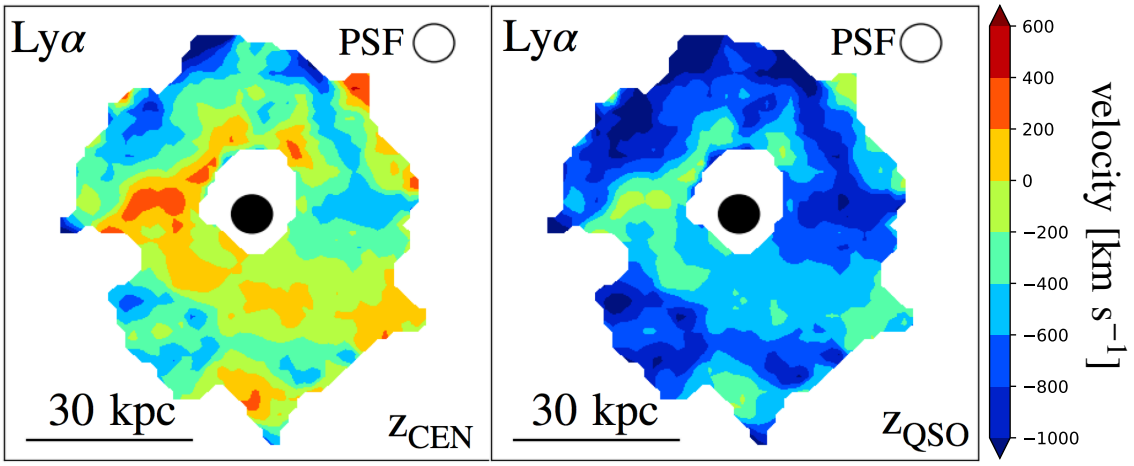

Fig. 7. Flux-weighted velocity maps of the Lyα-CEN for $S/N \geq 3$ regions relative to z_{CEN} (*left*) and to z_{QSO} (*right*).

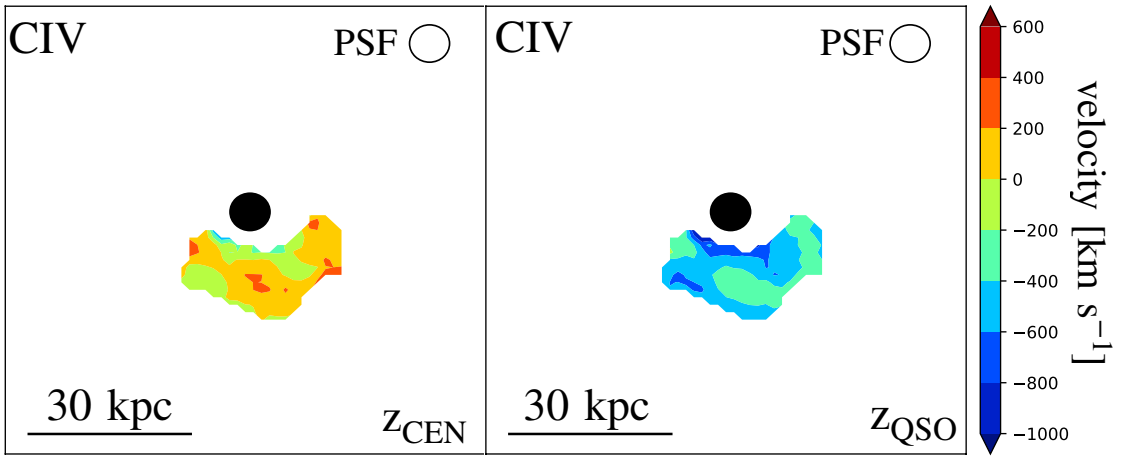

Fig. 8. Flux-weighted velocity maps for $S/N \geq 3$ regions of the CIV-CEN. As in Fig. 7, the *right and left panels* show the velocity relative to z_{CEN} and to z_{QSO}, respectively.

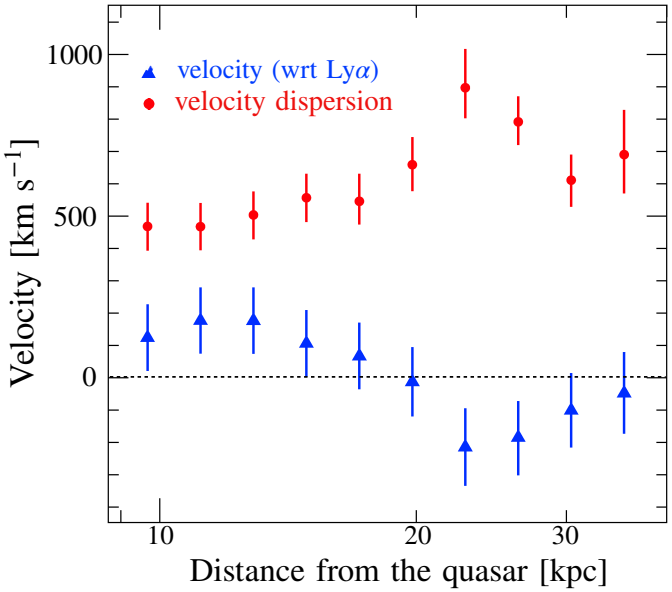

Fig. 9. Radial profile of velocity (blue triangles) and dispersion (red circles) derived from the modelling of a single Gaussian of the Lyα profiles extracted in concentric annular region centred on the quasar position.

(e.g. B16; AB19). The centroid of the narrow component corresponds to a redshift of $z \sim 3.562 \pm 0.001$, which is consistent with z_{QSO}.

5. Discussion

5.1. Comparison with the properties of other Lyα-CEN samples

We have reported the discovery of a Lyα-CEN around the hyperluminous RQQ J1538+08, which exhibits a projected size of ~150 kpc and a luminosity of $L_{Ly\alpha} \sim 2 \times 10^{44}$ erg s^{-1}. Previous MUSE studies at similar redshifts (i.e. $z \sim 3$–4) and exposures (0.75–1 h) reported Lyα-CEN around similarly luminous RQQs (B16) and quasars with slightly lower L_{bol} (AB19). The Lyα-CEN around J1538+08 exhibits a maximum projected size, which is similar to the average value (~150 kpc) found for the B16 sample, while its luminosity is one of the highest measured thus far (see Fig. 14) and it is comparable to the luminosity of the known ELANe (e.g, Cantalupo et al. 2014; Hennawi et al. 2015; Cai et al. 2017b; Arrigoni Battaia et al. 2018).

The $SB_{Ly\alpha}$ radial profile of our CEN, shown in Fig. 3, exhibits a projected distance from the quasar at a SB of ~10^{-18} erg s^{-1} cm^{-2} arcsec^{-2} (i.e. ~50 kpc), which is similar to the one inferred from the average profiles from B16 and AB19.

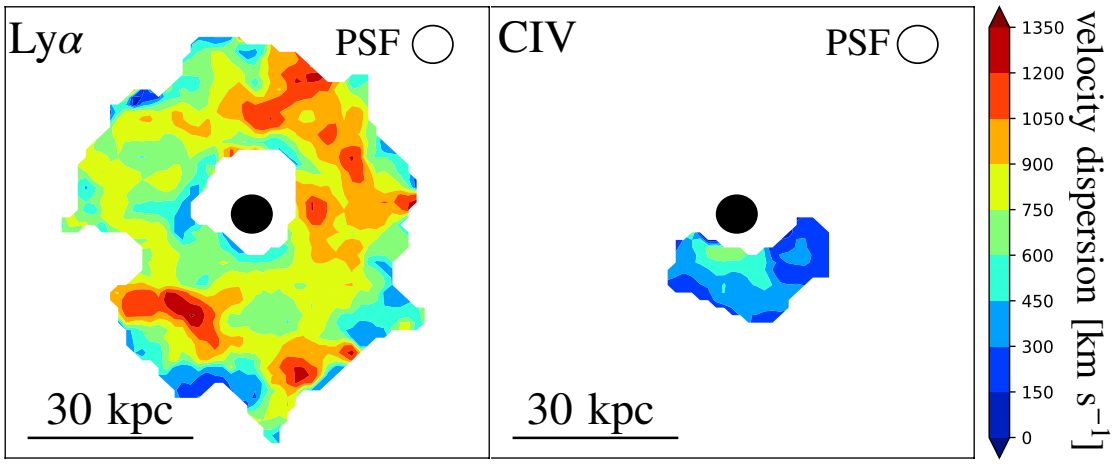

Fig. 10. Flux-weighted velocity dispersion maps for Lyα- (*left*) and CIV- (*right*) CEN. The MUSE spectral resolution in these dispersion maps is $\approx$70 km s^{-1}.

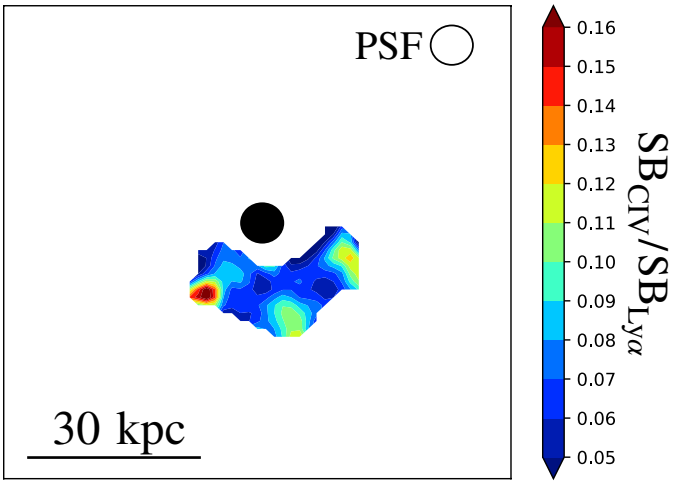

Fig. 11. Map of the CIV/Lyα SB ratio. Only regions with $S/N > 3$, for both the Lyα- and CIV-CEN, are displayed.

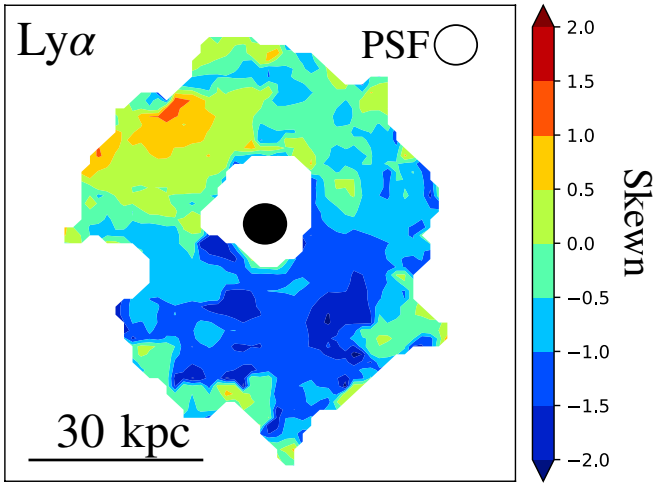

Fig. 12. Skewness map of the line profile of the Lyα-CEN.

This behaviour seems to be independent of the luminosity of the quasar (AB19). However, it is important to notice that the SB at this distance coincides with the level of the 2σ Poisson noise of the image and, therefore, deeper observations are needed in order to verify this claim.

Interestingly, some WISSH quasars are included in the B16 (J0124+00, J1621−00), AB19 (J0125−10, J0947+14), and Cai et al. (2019) (J2123−00) samples. The size and luminosity of the Lyα-CEN detected around them appear to be heterogeneous (see Fig. 14), suggesting that the properties of these CEN have no simple dependence on the similar, large quasar radiative output (i.e. $L_{\rm bol} > 10^{47}$ erg s^{-1}).

We also checked for possible dependencies on the RQQs bolometric and 2500 Å luminosities (derived from spectral energy distribution modelling; Duras et al. 2017, and in prep.) to verify if the nuclear radiative output could affect the properties of the Lyα-CEN around the WISSH quasars considered here. However, no significant trend with luminosity was observed, confirming the result reported by AB19 for a larger sample of quasars.

5.2. Kinematics of the Lyα- and CIV-CEN of J1538+08

From the velocity maps of the Lyα- and CIV-CEN (Figs. 7 and 8), no coherent kinematic structures that possibly hint at bulk motions and rotations were detected. However, the velocity map of the Lyα-CEN exhibits a large fraction (79^{+9}_{-10}%)[3] of pixels with $S/N \geq 3$ with negative velocities relative to $z_{\rm CEN}$. This can be justified by the presence of the additional blueshifted component in the Lyα line profile (see Sect. 4.5 and Fig. 2). For the CIV-CEN, where we did not detect any significant additional component, the velocity map shows a roughly equal number of pixels with negative and positive velocities. Interestingly, by adopting $z_{\rm QSO}$ as a reference redshift for the velocity maps of the Lyα- and CIV-CEN, we find that ~100% of the $S/N \geq 3$ pixels have negative velocities. Furthermore, our Lyα-CEN shows a peak with a negative velocity of -438 ± 267 km s^{-1}. This can be an indication that our $z_{\rm QSO}$ estimated from the Hβ may suffer from systematic uncertainties. Indeed, for a sample of 849 quasars, Shen et al. (2016) find that the determination of the quasar redshift from Hβ is subject to uncertainties as large as ~400 km s^{-1}. This can compensate the reported negative velocity offsets of the Lyα peak and the velocity distribution of the $S/N \geq 3$ pixels at levels of ~1–2σ.

Regarding the velocity dispersion, we measured a spatially averaged value $\bar{\sigma}_{\rm v} = 733 \pm 85$ km s^{-1} from the dispersion map (see Table 1). This is a factor of two larger than those measured

[3] Errors were derived from the uncertainties to the redshift of both the quasar and nebula.

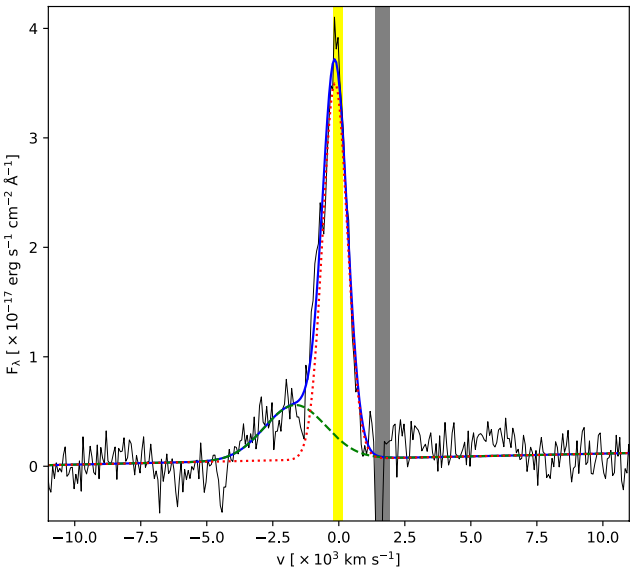

Fig. 13. Lyα spectrum extracted from the CEN region with $sk < -0.5$ and $S/N > 3$ and modelled (blue solid line) by two Gaussian components (red dotted and green dashed lines). Interestingly, the broad ($\sim$1170 km s^{-1}) wing is blueshifted by $\sim$1520 km s^{-1} from the narrow component. The grey area is not considered in the modelling as it includes a region contaminated by a sky feature. The yellow region reports the $\pm 1\sigma$ uncertainty on the z_{QSO}.

Table 2. Properties derived from the two-component Gaussian fit of the Lyα-CEN spectrum extracted from regions with $S/N \geq 3$ and $sk < -0.5$.

Components	Narrow	Broad
λ_{cen} [Å]	5546.3 ± 1.3	5518.3 ± 6.5
σ_v [km s^{-1}]	470 ± 70	1170 ± 260
Flux [a] [$\times 10^{-16}$ erg s^{-1} cm^{-2}]	7.4 ± 0.7	2.7 ± 0.9
v_{shift} [b]	(1520 ± 360) km s^{-1}	
v_{max} [c]	(3860 ± 870) km s^{-1}	
χ^2/d.o.f.	402/366	

Notes. [a]Integrated fluxes of the narrow and broad Gaussian components. [b]Velocity offset between the positions of the broad and narrow components. [c]Maximum velocity of the blueshifted, broad component defined as $v_{max} = v_{shift} + 2\sigma_v$, where σ_v is the dispersion derived for the broad component.

around the quasars of B16 and AB19 samples, which span the range of $\sigma_v \approx [200, 400]$ km s^{-1}. This value is more similar to the reported values for Lyα-CEN around high-z radio galaxies in the regions affected by radio jets ($\sigma_v \gtrsim 600$ km s^{-1}; van Ojik et al. 1997; Villar-Martín et al. 2003; Humphrey et al. 2006; Silva et al. 2018).

Interestingly, the dispersion map of the Lyα-CEN around J1538+08 reports several discrete and compact regions with very high $\sigma_v \approx 1000$ km s^{-1} at an average distance from the quasar of 20–30 kpc (see Fig. 10). These high σ_v regions could be due to the turbulence generated by continuum or line-emitting active sources at z_{CEN}, which possibly inject energy into the CGM. However, no continuum sources in the MUSE FOV are associated with high σ_v values within the Lyα-CEN. Similar to AB19, we used `CubExtractor` to search for Lyα emitters by setting $S/N_{th} > 5$ and $N_{min}^{vox} = 50$. We did not detect any source within the CEN. We only found a source with a flux of 3.5×10^{-16} erg s^{-1} cm^{-2}, at the redshift of the CEN ($z \approx 3.560$),

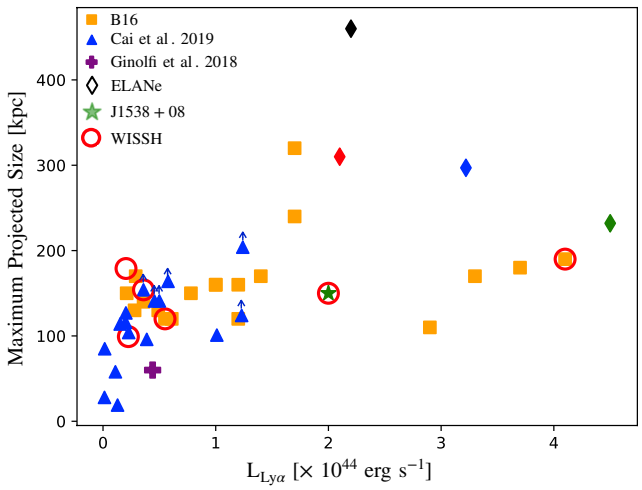

Fig. 14. Maximum projected size versus luminosity of the Lyα-CEN around J1538+08 (green star) and around quasars from the B16 (orange squares), Cai et al. (2019) (blue triangles) and Ginolfi et al. (2018) (purple cross) samples. The values for the ELANe (diamond symbols) detected by Cantalupo et al. (2014) (black), Hennawi et al. (2015) (red), Cai et al. (2017a) (green), and Arrigoni Battaia et al. (2018) (blue) are also included. WISSH quasars are marked with an additional red circle. We also report the two Lyα-CEN around the WISSH quasars from the AB19 sample, i.e. those with the lower luminosities. For these two Lyα-CEN, the maximum distance from the quasar spanned by the Lyα emission within the 2σ isophote multiplied by a factor of two is shown since AB19 do not report the values of the maximum projected size.

outside its boundaries and at a projected distance of $\sim$250 kpc from the quasar (RA = 15:38:28.7, Dec = +8:55:00.80), which very likely cannot affect the nebular emission.

5.3. Metals in CGM

The CIV-CEN revealed around J1538+08 is one of the few extended (75 kpc) CIV-emitting regions detected at high significance (5σ)[4] and spatially mapped around a RQQ. This provides a clear indication of a metal enriched medium (i.e. non-pristine) around this quasar. The luminosity of this CEN ($L_{CIV} \simeq 10^{43}$ erg s^{-1}) is comparable to those measured for CIV-CEN detected around radio galaxies at similar redshift (Villar-Martín et al. 2007a). However, its morphology shows a marked asymmetry relative to the central quasar position. This is at odds with symmetrically distributed CEN reported around radio galaxies (e.g. Villar-Martín et al. 2007b; Silva et al. 2018). Interestingly, the ratio between the SB radial profiles of the CIV and Lyα reported in Fig. 6 (i.e. in the southern wedge containing the SB Lyα peak and the CIV-CEN) is a factor of $\sim$0.1 and is constant up to $\sim$25 kpc (i.e. the distance where the Poisson noise starts to dominate the CIV-CEN radial profile). This evidence and the spatial co-location of the SB peaks of the two CEN suggest that they could trace the same gas and, hence, be triggered by the same mechanism. Deeper observations would hopefully reveal fainter CIV emission with the same size and morphology of the Lyα-CEN in J1538+08.

5.4. Powering mechanisms for the Lyα CEN

The possible powering mechanisms of the Lyα-CEN include quasar photoionisation (i.e. fluorescence), collisional excitation

[4] This value represents the integrated S/N computed for the extended CIV emission line.

(i.e. cooling), and shocks. In the case of fluorescence, assuming that the quasar is surrounded by cold and spherical clouds, we can estimate the CEN SB in the following two extreme regimes: optically thin (with a column density of $N_{\rm H} \ll 10^{17.2}\,{\rm cm}^{-2}$) and optically thick ($N_{\rm H} \gg 10^{17.2}\,{\rm cm}^{-2}$; Hennawi & Prochaska 2013). We obtain $\mathrm{SB}^{\rm thick}_{{\rm Ly}\alpha} \simeq 2.8 \times 10^{-15}\,{\rm erg\,s\,cm^{-2}\,arcsec^{-2}}$ and $\mathrm{SB}^{\rm thin}_{{\rm Ly}\alpha} \simeq 2.2 \times 10^{-18}\,{\rm erg\,s\,cm^{-2}\,arcsec^{-2}}$, for optically thick[5] and optically thin[6] gas, respectively. In our case, we find that $\mathrm{SB}_{{\rm Ly}\alpha}$ for regions with $S/N \geq 3$ is $\simeq 2.3\times10^{-17}\,{\rm erg\,s\,cm^{-2}\,arcsec^{-2}}$. This value is more compatible with $\mathrm{SB}^{\rm thin}_{{\rm Ly}\alpha}$ than with $\mathrm{SB}^{\rm thick}_{{\rm Ly}\alpha}$, supporting the presence of an optically thin medium as already reported in previous works (e.g. AB19; Cai et al. 2019).

The CIV/Lyα and HeII/Lyα ratios could be used to understand if shocks or collisional excitation are viable powering mechanisms for the observed Lyα-CEN (but see Cantalupo et al. 2019). The detection of the CIV-CEN allows us to rule out cooling due to gravitational accretion as the powering mechanism of this CEN. However, it is notoriously difficult to disentangle photoionisation models from shock models in a HeII/Lyα versus CIV/Lyα diagram (Arrigoni Battaia et al. 2015a). Nevertheless, photoionisation models usually do not predict lower levels of HeII/Lyα with respect to CIV/Lyα (e.g. Humphrey 2019; Cantalupo et al. 2019). On the contrary, they predict ratios of the same order for the two transitions. This is because these two emission lines have similar ionisation energies, 64.5 eV for CIV and 54.4 eV (4 Ryd) for HeII. On the other hand, shock models (Allen et al. 2008) do show cases in which the HeII/Lyα ratio is lower than the CIV/Lyα ratio. Indeed, according to shock and precursors models presented by Allen et al. (2008) and Arrigoni Battaia et al. (2015b) regarding the origin of extended nebular emission, the values of CIV/Lyα and HeII/Lyα inferred from our analysis are consistent with a shock propagating at 200–300 km s^{-1} in a $n_{\rm H} \sim 10{-}100\,{\rm cm^{-3}}$ gas or with a faster >1000 km s^{-1} shock in a denser gas ($n_{\rm H} > 100\,{\rm cm^{-3}}$). If we assume that the $v_{\rm shift} = 1520\,{\rm km\,s^{-1}}$ is the velocity of the shock, then the emitting gas is required to be at high densities ($n_{\rm H} > 100\,{\rm cm^{-3}}$).

The aforementioned photoionisation and shock models do not include a contribution from resonant scattering of Lyα photons from the quasar. In a case in which such a contribution is important, the CIV/Lyα and HeII/Lyα ratios predicted by those models need to be corrected and shifted to lower values. However, it has been shown that the efficient diffusion in velocity space allows the Lyα resonantly scattered photons, which were produced by the quasar itself, to escape the system at very small scales of <10 kpc (Dijkstra et al. 2006). Therefore, this should result in a negligible contribution of scattered Lyα emission on scales >10 kpc (e.g, Cantalupo et al. 2014). A firm characterisation of the Lyα resonant scattering contribution requires a full radiative transfer calculation on a three dimensional gas distribution that represents this system. This approach is beyond the scope of this work.

5.5. Evidence of outflowing gas in the CGM

The blueshifted broad component in the Lyα spectrum of the CEN provides tantalising evidence for the presence of outflowing gas reaching a projected distance of 20–30 kpc from the quasar, that is, into the CGM surrounding J1538+08. The latter also exhibits a host-galay scale [OIII] outflow with a mass outflow rate of $\sim 530\,M_\odot\,{\rm yr^{-1}}$, a maximum velocity of $\sim$2900 km s^{-1}, and kinetic power of $\dot{E}_{\rm kin} = 1.4\times10^{45}\,{\rm erg\,s^{-1}}$ (see Vietri et al. 2018). In an energy conserving scenario in which the large-scale outflow reported in this paper is in the later stage of the AGN-driven [OIII] one (e.g. Bischetti et al. 2017; Vietri et al. 2018), by assuming an expansion at $v_{\rm out} = v_{\rm shift} \sim 1500\,{\rm km\,s^{-1}}$, we estimated a mass outflow rate of $\dot{M}_{\rm out} \simeq 300\,M_\odot\,{\rm yr^{-1}}$, which is comparable to the [OIII] one. It is important to notice that, assuming $v_{\rm out} = 300\,{\rm km\,s^{-1}}$ as suggested by the CIV/Lyα and HeII/Lyα values in shock+precursor models, (see Sect. 5.3) we would obtain a $\dot{M}_{\rm out}$ that is larger by a factor of 25 but that is still comparable with the typical $\dot{M}_{\rm out}$ reported for [OIII] outflows in the WISSH sample (Bischetti et al. 2017). By assuming a constant velocity of 1500 km s^{-1} (see Table 2), we estimated that an outflow at host galaxy scales (i.e. ~5–10 kpc Bischetti et al. 2017) would take ~7–13 Myr to reach the distance of our CGM outflow (i.e. ~30 kpc). In adopting a velocity of ~300 km s^{-1}, we would obtain an upper limit to the outflow time a factor of 5 larger than the previous estimate.

The sudden increase of the velocity dispersion of the Lyα-CEN to $\sigma_{\rm v} \sim 900\,{\rm km\,s^{-1}}$ at a distance of ~20 kpc (see Fig. 9) could be partially due to the presence of the outflow component and hence to an incorrect parameterisation of the line profile with a single Gaussian component. Unfortunately the S/N of our observations did not allow us to recompute the radial profile of the v and $\sigma_{\rm v}$ of the Lyα line using a two-component Gaussian modelling because the S/N of the broad Lyα line in each bin is too low. Deeper MUSE observations are therefore needed to verify the presence of a broad and blueshifted component over the entire Lyα-CEN and assess if the CIV-CEN also shares the same kinematics.

Given the resonant nature of the Lyα transition, complex radiative transfer models that account for the velocity field, the density structure of the CEN, and the geometry of the radiation field are needed in order to properly interpret the properties derived by the Lyα line profile fitting (e.g. Cantalupo et al. 2005; Gronke & Dijkstra 2016). It is worth noting that the presence of an expanding shell surrounding the quasar, assuming spherical symmetry and isotropic geometry of the photoionising radiation field, may produce an asymmetric double peak profile in which the blue-ward component is strongly suppressed (Verhamme et al. 2006; Laursen et al. 2009; Steidel et al. 2010; Chung et al. 2019). This would provide support to the hypothesis of an outflowing CEN whose two components of the Lyα profile are associated with the same expanding gas. It is important to notice that in this simple model (i.e. symmetric, homogeneous, and isotropic gas distribution), the main peak component is always on the red side compared to the systemic redshift of the CEN. However, assuming that $z_{\rm QSO} \equiv z_{\rm CEN}$, our Ly$\alpha$-CEN does not show such a red line component (see Fig. 13). To test the nature of this putative outflow in the context of an asymmetric, inhomogeneous gas distribution, MUSE observations with a higher S/N are needed along with a more accurate determination of $z_{\rm QSO}$ (e.g. from the CO line) and radiative transfer models.

6. Summary and conclusions

In this paper we have presented a VLT/MUSE investigation on the CGM around J1538+08, a $z \approx 3.6$, broad-line, RQQ belonging to the WISSH quasars sample (Bischetti et al. 2017). The main results can be summarised as follows.

[5] The luminosity at the Lyman edge, which is required by the formula (15) by Hennawi & Prochaska (2013), has been estimated by the L_{1450} (see Duras et al., in prep.) as detailed in Lusso et al. (2015) and Farina et al. (2019). Moreover, we adopted as a CEN radius, 40 kpc (see Fig. 3) and a covering factor $f_{\rm c} = 0.5$.

[6] We used the formula (10) in Hennawi & Prochaska (2013) and adopted the following fiducial values: $N_{\rm H} = 10^{20}\,{\rm cm^{-2}}$, density $n_{\rm H} = 0.1\,{\rm cm^{-3}}$, and $f_{\rm c} = 0.5$.

– We discovered a CGM emission nebula (CEN) detected in Lyα of ∼150 kpc surrounding J1538+08, which is among the most luminous Lyα-CEN ($\sim 2 \times 10^{44}$ erg s^{-1}) reported so far (Borisova et al. 2016; Arrigoni Battaia et al. 2019; Farina et al. 2019). Our nebula appears roughly symmetric on large scales (several tens of kiloparsecs) and exhibits a bright SB peak located at ∼10−15 kpc southwards of the quasar.
– We obtained one of the first 2D-mappings of a significantly detected (∼5σ), extended (∼75 kpc) CIV-CEN around a RQQ. Given its spatial coincidence with the Lyα SB peak and a similar SB profile, it is very likely associated with the Lyα-CEN.
– We find no significant velocity pattern in the kinematics of the Lyα-CEN. Remarkably, the average velocity dispersion $\bar{\sigma}_v \simeq 700$ km s^{-1} is higher than the typical values measured in RQQs and it is notably more similar to the dispersion observed for Lyα-CEN around high-redshift radio galaxies (van Ojik et al. 1997; Villar-Martín et al. 2003; Humphrey et al. 2006; Silva et al. 2018) and outflow-dominated systems (Ginolfi et al. 2018).
– We obtained one of the first 2D characterisation via IFU spectroscopy of an ionised outflow at CGM scales (≫10 kpc) around a RQQ by performing the spectral analysis of an extended region with a negative skewness value.
Specifically, the analysis of the skewness map of the Lyα-CEN reveals a region within 30 kpc that is to the south of the quasar in which the skewness is negative (see Fig. 12); additionally, the Lyα emission profile is significantly asymmetric with a blue tail. This region roughly overlaps with the SB peak of the Lyα-CEN and includes the CIV-CEN.
The Lyα spectrum that was extracted from the region showing negative skewness is well modelled with two Gaussian components (Fig. 13). This fit resulted into a systemic narrow ($\sigma_v \sim 500$ km s^{-1}) component and a broader ($\sigma_v \approx 1200$ km s^{-1}) one. The latter is blueshifted by $v_{shift} \simeq 1500$ km s^{-1} and is indicative of outflowing gas on CGM-scales.

All of the reported results clearly indicate the presence of a metal-enriched (i.e. non pristine) gas with kinematic features that are consistent with an outflowing gas component at scales of tens of kiloparsecs. Both deeper spatially resolved spectroscopic observations of the CGM around this hyper-luminous quasar and dedicated radiative transfer modellings are necessary in order to confirm and refine this scenario. Specifically, they are needed to accurately characterise the CEN and outflow physical properties and understand the role of the outflow in transporting metals in the CGM.

Acknowledgements. We thank Laura Pentericci, Fabrizio Nicastro, Emanuele Giallongo and Marco Stangalini for useful discussions. We thank Gabriele Pezzulli for providing us with the surface brightness radial profile of J0124+00. LZ, EP acknowledge financial support under ASI/INAF contract 2017-14-H.0. FF, EP, AB and CF acknowledge financial support from PRIN-INAF-2016 FORECAST. This research has made use of the NASA/IPAC Extragalactic Database (NED), which is operated by the Jet Propulsion Laboratory, California Institute of Technology, under contract with the National Aeronautics and Space Administration. SC gratefully acknowledges support from Swiss National Science Foundation grant PP00P2_163824.

References

Allen, M. G., Groves, B. A., Dopita, M. A., Sutherland, R. S., & Kewley, L. J. 2008, ApJS, 178, 20
Arrigoni Battaia, F., Hennawi, J. F., Prochaska, J. X., & Cantalupo, S. 2015a, ApJ, 809, 163
Arrigoni Battaia, F., Yang, Y., Hennawi, J. F., et al. 2015b, ApJ, 804, 26
Arrigoni Battaia, F., Hennawi, J. F., Cantalupo, S., & Prochaska, J. X. 2016, ApJ, 829, 3
Arrigoni Battaia, F., Chen, C.-C., Fumagalli, M., et al. 2018, A&A, 620, A202
Arrigoni Battaia, F., Hennawi, J. F., Prochaska, J. X., et al. 2019, MNRAS, 482, 3162
Bacon, R., Accardo, M., Adjali, L., et al. 2010, in Ground-based and Airborne Instrumentation for Astronomy III, SPIE Conf. Ser., 7735, 773508
Bacon, R., Conseil, S., Mary, D., et al. 2017, A&A, 608, A1
Bischetti, M., Piconcelli, E., Vietri, G., et al. 2017, A&A, 598, A122
Bischetti, M., Piconcelli, E., Feruglio, C., et al. 2018, A&A, 617, A82
Borisova, E., Cantalupo, S., Lilly, S. J., et al. 2016, ApJ, 831, 39
Bruni, G., Piconcelli, E., Misawa, T., et al. 2019, A&A, 630, A111
Cai, Z., Fan, X., Bian, F., et al. 2017a, ApJ, 839, 131
Cai, Z., Fan, X., Yang, Y., et al. 2017b, ApJ, 837, 71
Cai, Z., Cantalupo, S., Prochaska, J. X., et al. 2019, ApJS, 245, 23
Cantalupo, S. 2017, in Gas Accretion onto Galaxies, eds. A. Fox, & R. Davé, Astrophys. Space Sci. Lib., 430, 195
Cantalupo, S., Porciani, C., Lilly, S. J., & Miniati, F. 2005, ApJ, 628, 61
Cantalupo, S., Arrigoni-Battaia, F., Prochaska, J. X., Hennawi, J. F., & Madau, P. 2014, Nature, 506, 63
Cantalupo, S., Pezzulli, G., Lilly, S. J., et al. 2019, MNRAS, 483, 5188
Christensen, L., Jahnke, K., Wisotzki, L., & Sánchez, S. F. 2006, A&A, 459, 717
Chung, A. S., Dijkstra, M., Ciardi, B., Kakiichi, K., & Naab, T. 2019, MNRAS, 484, 2420
Dijkstra, M., Haiman, Z., & Spaans, M. 2006, ApJ, 649, 37
Duras, F., Bongiorno, A., Piconcelli, E., et al. 2017, A&A, 604, A67
Farina, E. P., Arrigoni-Battaia, F., Costa, T., et al. 2019, ApJ, 887, 196
Faucher-Giguère, C.-A., & Quataert, E. 2012, MNRAS, 425, 605
Fiore, F., Feruglio, C., Shankar, F., et al. 2017, A&A, 601, A143
Ginolfi, M., Maiolino, R., Carniani, S., et al. 2018, MNRAS, 476, 2421
Gronke, M., & Dijkstra, M. 2016, ApJ, 826, 14
Heckman, T. M., Lehnert, M. D., Miley, G. K., & van Breugel, W. 1991, ApJ, 381, 373
Hennawi, J. F., & Prochaska, J. X. 2013, ApJ, 766, 58
Hennawi, J. F., Prochaska, J. X., Cantalupo, S., & Arrigoni-Battaia, F. 2015, Science, 348, 779
Hogan, C. J., & Weymann, R. J. 1987, MNRAS, 225, 1P
Humphrey, A. 2019, MNRAS, 486, 2102
Humphrey, A., Villar-Martín, M., Fosbury, R., Vernet, J., & di Serego Alighieri, S. 2006, MNRAS, 369, 1103
Humphrey, A., Villar-Martín, M., Fosbury, R., et al. 2007, MNRAS, 375, 705
Humphrey, A., Vernet, J., Villar-Martín, M., et al. 2013, ApJ, 768, L3
Laursen, P., Sommer-Larsen, J., & Andersen, A. C. 2009, ApJ, 704, 1640
Lusso, E., Worseck, G., Hennawi, J. F., et al. 2015, MNRAS, 449, 4204
Lusso, E., Fumagalli, M., Fossati, M., et al. 2019, MNRAS, 485, L62
Marino, R. A., Cantalupo, S., Pezzulli, G., et al. 2019, ApJ, 880, 47
Menci, N., Fiore, F., Feruglio, C., et al. 2019, ApJ, submitted [arXiv:1904.07621]
Møller, P., & Warren, S. J. 1998, MNRAS, 299, 661
Planck Collaboration VI. 2018, A&A, submitted [arXiv:1807.06209]
Shen, Y., Brandt, W. N., Richards, G. T., et al. 2016, ApJ, 831, 7
Silva, M., Humphrey, A., Lagos, P., et al. 2018, MNRAS, 474, 3649
Steidel, C. C., Erb, D. K., Shapley, A. E., et al. 2010, ApJ, 717, 289
Taniguchi, Y., & Shioya, Y. 2000, ApJ, 532, L13
van Ojik, R., Roettgering, H. J. A., Miley, G. K., & Hunstead, R. W. 1997, A&A, 317, 358
Verhamme, A., Schaerer, D., & Maselli, A. 2006, A&A, 460, 397
Vietri, G., Piconcelli, E., Bischetti, M., et al. 2018, A&A, 617, A81
Villar-Martín, M., Vernet, J., di Serego Alighieri, S., et al. 2003, in Rev. Mex. Astron. Astrofis. Conf. Ser., eds. V. Avila-Reese, C. Firmani, C. S. Frenk, & C. Allen, 17, 260
Villar-Martín, M., Sánchez, S. F., Peletier, R., et al. 2006, Astron. Nachr., 327, 187
Villar-Martín, M., Humphrey, A., De Breuck, C., et al. 2007a, MNRAS, 375, 1299
Villar-Martín, M., Sánchez, S. F., Humphrey, A., et al. 2007b, MNRAS, 378, 416
Weidinger, M., Møller, P., & Fynbo, J. P. U. 2004, Nature, 430, 999
Weidinger, M., Møller, P., Fynbo, J. P. U., & Thomsen, B. 2005, A&A, 436, 825
Weilbacher, P. M., Streicher, O., Urrutia, T., et al. 2014, in Astronomical Data Analysis Software and Systems XXIII, eds. N. Manset, & P. Forshay, ASP Conf. Ser., 485, 451
Wilman, R. J., Johnstone, R. M., & Crawford, C. S. 2000, MNRAS, 317, 9

Appendix A: Stellar contamination

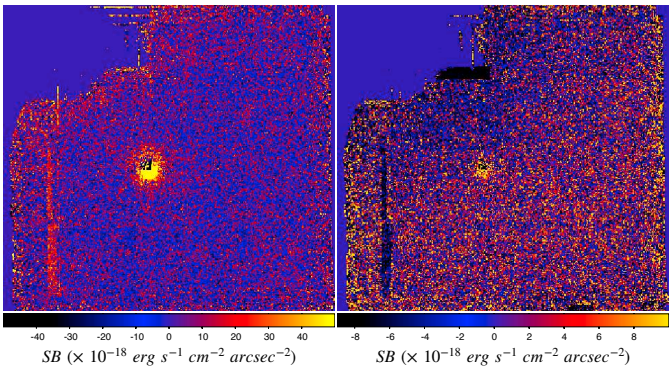

Fig. A.1. Images obtained by collapsing the final PSF- and continuum-subtracted datacubes in the spectral regions of Lyα- (*left panel*) and CIV-CEN (*right panel*), respectively. The homogeneous blue area on the upper-left corner represents the mask applied to the exposures during the data reduction in order to exclude the saturated stellar flux in the FOV.

Figure A.1 reports the image of the MUSE FOV that was obtained by collapsing the spectral region of the Lyα- (left) and CIV- (right) CEN in the PSF- and continuum-subtracted datacube. The upper-left corner of each image represents the region that is contaminated by the luminous star, which was masked during the data reduction. A visual inspection reveals no residual contamination at the CEN position. We performed a more quantitive estimation by measuring the average flux in concentric annular regions centred on the star. We found no significant stellar contamination on the nebular emissions. The average contamination was estimated in concentric annuli with respect to the centre of the star by excluding the nebular region. We estimated a stellar contamination of the order of ∼11%, ∼6%, and ∼6% in the north and south Lyα-CEN regions and over the entire CIV-CEN, respectively.

Appendix B: Blue tail

In this Appendix we report on several tests we performed in order to check for possible contamination of the weak CEN emission from the bright quasar emission line residuals after the Lyα subtraction. The left panel of Fig. B.1 shows the SB emission of the more blueshifted portion of the blue tail (i.e. highlighted in red in the right panel). This was obtained by collapsing the spectral region including the wing of the blue tail in order to avoid any possible contamination of the narrow Lyα component. To remove possible residuals at each pixel, we applied a subtraction of the continuum, which was measured from the spectral region highlighted in green in Fig. B.1. The final pseudo-NB image exhibits an asymmetric shape with respect to the quasar position and it is spatially associated with the peak of the SB of the Lyα-CEN. In case of residual AGN contribution, we would have expected a symmetric emission around the quasar. This provides an indication that the blue tail is not the result of emission line contamination from the quasar Lyα.

We find that the average intensity of the PSF subtraction residuals are three times lower than the intensity of the blue tail, which is, moreover, spatially coincident with a high S/N region. We further checked the quasar emission line contamination by inspecting the region of the bright quasar SiIV emission line. We measured the PSF-subtracted radial profile of the slope of the blue tail at the wavelength of the SiIV line. We found a flat radial profile with an average value around zero. This provides a further indication that the quasar emission does not contribute to the blue tail emission and, hence, that this is a genuine and intrinsic emission of the CEN.

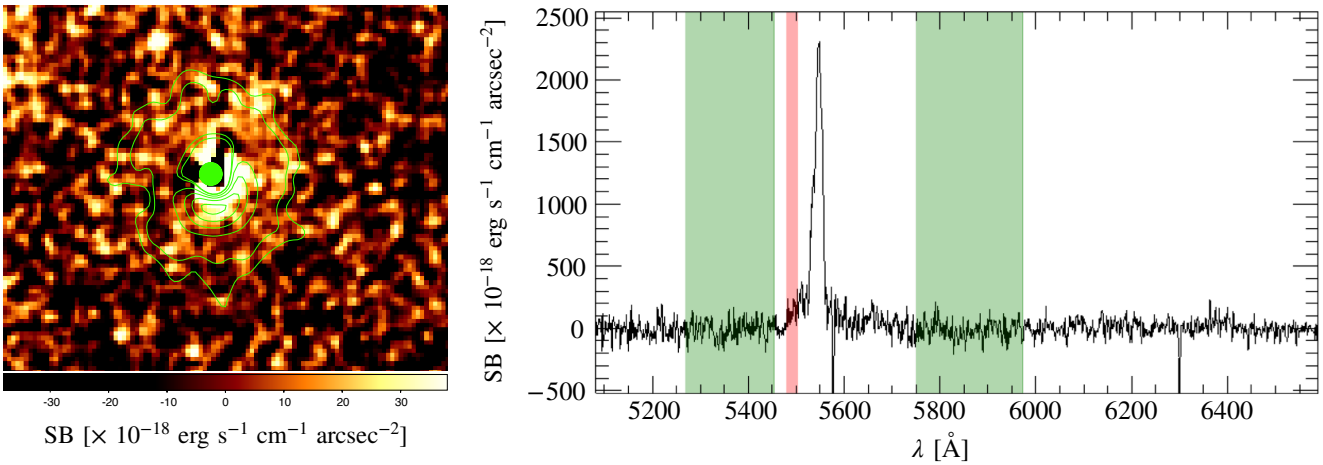

Fig. B.1. *Left panel*: pseudo-NB image obtained by collapsing the spectral region of the blue tail (see red area in the *right panel*) and by subtracting the continuum estimated in spectral regions without line features (see green areas in the *right panel*). *Right panel*: spectrum that is extracted from the PSF- and continuum-subtracted datacube by only selecting the spaxels that belong to the CEN with $S/N > 5$. The red and green areas mark the spectral region that is collapsed and subtracted, respectively, to obtain the pseudo-NB in the *left panel*.